Graphical Abstract

Drivers of spectro-temporal variability in multi-spectral soil reflectance measured from space - A continental-scale analysis

Paul Karlshoefer, Christine Alewell, Pablo d'Angelo, Uta Heiden

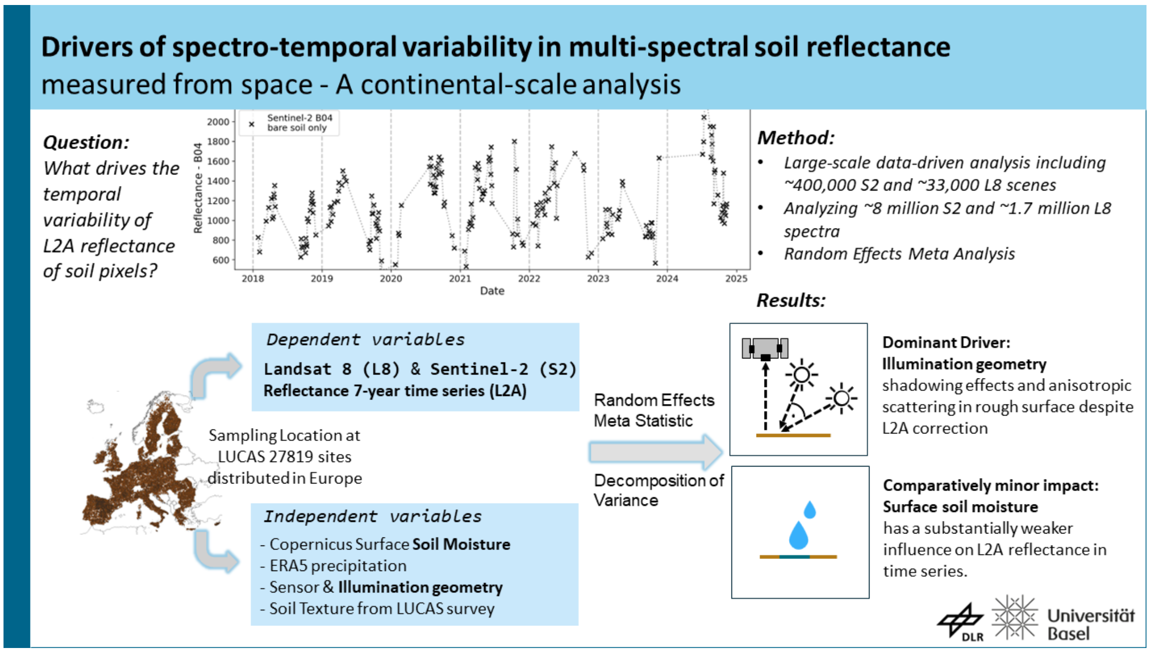

Highlights

Drivers of spectro-temporal variability in multi-spectral soil reflectance measured from space - A continental-scale analysis

Paul Karlshoefer, Christine Alewell, Pablo d'Angelo, Uta Heiden

- Continental-scale analysis of temporal variability in soil reflectance
- Parallel Sentinel-2 and Landsat 8 analysis at 27,819 sites over 7 years
- Seasonal Changes in sun zenith angle has strong effect via surface shadowing
- Variance decomposition reveals that surface soil moisture is less of a factor
- Soil texture influences spectral sensitivity to moisture and illumination

Drivers of spectro-temporal variability in multi-spectral soil reflectance measured from space - A continental-scale analysis

Paul Karlshoefer[a,b], Christine Alewell[b], Pablo d'Angelo[a], Uta Heiden[a]

[a] *Remote Sensing Technology Institute German Aerospace Center Germany*
[b] *Department of Environmental Geosciences University Basel Switzerland*

Abstract

In Europe, bare soil is typically exposed only during short time windows and optical sensing by satellite constellations, such as Sentinel-2 and Landsat, therefore commonly rely on aggregates of soil reflectance spectra over extended periods of time. Depending on the length of the time series, substantial spectral variability can be observed in the soil spectra. To select appropriate aggregation strategies, it is critical to understand the mechanisms that drive temporal variability in soil reflectance.

In this study, we quantify the variance induced into soil reflectance time series by two properties that modify the spectral response: Surface soil moisture and the illumination geometry. We analyze seven-year time series of surface reflectance (Level-2A corrected) satellite imagery of Landsat 8 and Sentinel-2 at 27,819 LUCAS sites distributed across the European continent. The sites are correlated with independent datasets from Copernicus and ECMWF. A rigorous statistical framework is applied to estimate the global sensitivity for both properties, using pooled standardized effect sizes ($\bar{\beta}^*$) and its isolated contribution to spectral variance, using pooled partial eta squared ($\bar{\eta}_P^2$) for each spectral band. Furthermore, we explicitly separate illumination effects attributable to atmospheric influences (e.g. haze, dust, light-scattering) from those arising from ground-level surface–light interactions (e.g. shadows cast in rough surfaces at shallow elevation angles).

Results show that the dominant driver of temporal variability in measured soil reflectance is the interaction between the rough bare soil surface and changes in solar incidence angle ($\bar{\eta}_P^2 \approx 0.2$) throughout the entire spectral domain. In contrast, surface soil moisture plays a comparatively minor role at all bands ($\bar{\eta_P^2} \approx 0.06$). The large volume of data further enables a stratified analysis by soil texture, revealing that soils with different textural properties respond with varying strength to both drivers. For example, the reflectance of clay-rich soils is influenced stronger by changes in the illumination geometry. Further, soils with a high content of sand tend to exhibit a weaker response to soil moisture than finer-textured soils with a greater

water-holding capacity.
The presented variance decomposition enables both, the implementation of targeted corrective measures, such as soil-specific BRDF corrections, and the exploitation of variability patterns caused by different soil aggregates themselves as proxies for soil property modeling.

Keywords:
surface soil moisture, BRDF, time series, bare surface, multi-spectral, Sentinel-2, Landsat 8

---

1. Introduction

Soils play a pivotal role in terrestrial ecosystems and are of fundamental importance for humanity, as approximately 95 % of the global food production stems from soils(UN, 2024). Intensified agricultural practices and ongoing climate change accelerate soil degradation, increasing the demand for reliable methods to monitor soil conditions and properties as well as map their trends on a large scale (Mulder et al., 2011).

Spaceborne multi-spectral sensors, such as Sentinel-2 and Landsat 8, are specifically designed for systematic, repeated, and radiometrically calibrated observations of Earth's surface, enabling large-scale and temporally continuous analyses. With equatorial repetition rates of 5 days (Sentinel-2 constellation, (ESA, 2015)) and 16 days (Landsat 8, (USGS, 2019)) and even less at higher latitudes, these sensors offer the possibility to observe soils that are exposed only a fraction of the time in a year. Over recent years, these data archives have expanded substantially, allowing the generation of specialized temporal composites that isolate pixels representing bare soil surfaces free from vegetation cover. In Europe, these conditions typically occur only intermittently due to natural processes and agricultural management practices, such as tillage, which temporarily remove vegetation cover and expose the underlying soil surface. These datasets (Broeg et al., 2025; Heiden et al., 2024; Rogge et al., 2018; Demattê et al., 2025; Heiden et al., 2022; Vaudour et al., 2021) provide insights on bare-surface and soil reflectance by aggregating all corresponding pixels over time-spans of up to multiple years.
Figure 1 illustrates this variability in the measured soil reflectance using the standard deviation through time of Sentinel-2's red band reflectance (B04) over a five-year period as published in Heiden et al. (2024). Thus each pixel represents the temporal variability at its location in all bare soil observations over five years.
Distinct spatial patterns are visible across multiple scales. At the continental scale,

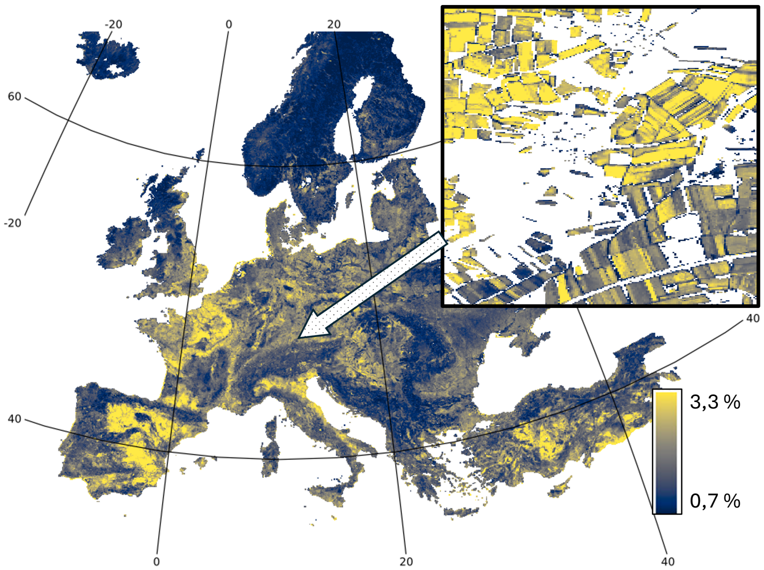

Figure 1: The figure shows the standard deviation of bare surface reflectance in the Sentinel-2 B04 band over a five-year period. The zoomed in cutout illustrates how the data is structured close-up and shows a region in Bavaria, Germany.

certain regions exhibit systematically higher variance. At local scales, neighboring agricultural fields often display different levels of variance, suggesting potential links to farming or land management practices. Even within individual fields spatial differences can be observed. Pixels located near field boundaries generally show lower variance than interior pixels.

Across the European continent, the average bare soil reflectance of Band B04 measured in the SoilSuite Europe is 11.7% (1170 L2A reflectance units in Sentinel-2), with an average temporal standard deviation of 1.75 percent points. This corresponds to a coefficient of variation on average of roughly 0.15 in the soil observations, suggesting that soil reflectance exhibit substantial variance for surfaces that have generally relatively stable spectral properties.

The temporal variability of soil reflectance is likely driven by a combination of environmental and other factors. To correctly interpret satellite-derived soil reflectance and related products, it is essential to understand the dominant processes contributing to this variance.

In addition to the spatial patterns discussed above, soil reflectance also exhibits a clear temporal structure (Figure 2). The time series of a randomly selected Sentinel-

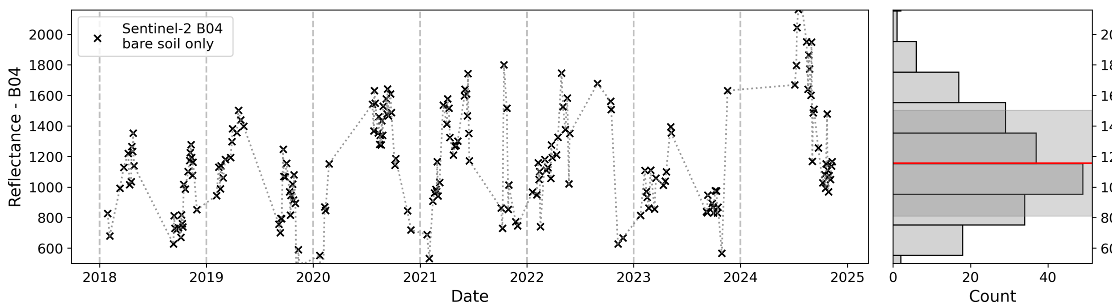

Figure 2: Variability in the bare soil reflectance of a pixels in the Band B04 in Sentinel-2 over 7 years (here LUCAS site 49382698). On the right, the distribution of soil pixels, its mean (red line at 1155 units) and the ±1 standard deviation (gray area, 347 units) is visualized.

2 pixel (red band, B04) shows that reflectance values classified as bare soil vary through time in a structured manner rather than appearing as independent observations. The red band was chosen for the illustration, but similar temporal patterns are observed across the entire spectral domain.

In such cases, the composite datasets that provide averaged reflectance per pixel provide only an incomplete description of the data (Box et al., 2015). Understanding the underlying processes of this variability may therefore require the consideration of temporal dependencies between successive observations.

Changes of the soil that alter the spectral signature generally require long time scales. For example, Fernández-Ugalde et al. (2020) report measurable changes in chemical soil properties like soil organic carbon "vary slowly over time" and change requires multiple years to become detectable in the spectrum. In contrast, physical properties, such as soil water content, change more rapidly. Moreover, uncertainties associated with satellite-based measurements of bare soil reflectance introduce additional sources of variability, taking place at similarly short time scales.

We selected two candidates in this study and focus on quantifying the contribution of these candidates to the temporal variability observed in satellite-derived soil reflectance. The first one is soil water content, which is a well-established driver of soil reflectance variability and can be considered a physical soil property. Both laboratory experiments (Lobell and Asner, 2002; Lesaignoux et al., 2013) and satellite-based observations (Mu et al., 2023; Sadeghi et al., 2017) consistently demonstrate an inverse relationship between soil moisture and reflectance across the visible to shortwave infrared spectral domain. This relationship has been shown to be sufficiently robust to enable the estimation of surface soil moisture from soil reflectance (McGuirk and Cairns, 2024), although the authors noted that this approach is not necessarily applicable to soils in general.

While the effect of moisture on reflectance is well understood in isolation and it is recognized as a factor which has to be considered in compositing workflows (Vaudour et al., 2021; Castaldi et al., 2019), its contribution to temporal variability in satellite-derived reflectance time series remains insufficiently constrained. In particular, the requirement for clear-sky conditions might introduce survivor bias, as successful observations are more likely during dry periods, which could restrict the impact of wet spectra.

Another factor that may systematically influence observed reflectance is the illumination geometry at the time of acquisition, here described mainly by the sun zenith or incidence angle and its interaction with the rough surface of bare soil. Operational Level-2A processors, such as those applied in Sentinel-2 or Landsat 8, include corrections for illumination-related and atmospheric effects associated with varying illumination geometry (Louis, 2021; U.S. Geological Survey, 2025). However, these approximations rely on general assumptions, designed to work on a large variety of surface types and it is insufficiently quantified to which extent residual illumination effects and cascading effects, such as surface-light interactions, propagate systematically into the retrieved surface reflectance of soil pixels. Furthermore, the influence of illumination geometry on the reflectance of rough surfaces has been demonstrated under controlled conditions at small scales using sand surfaces with varying roughness (Bachmann et al., 2014; Badura and Bachmann, 2019). Plowed or otherwise rough soils respond differently to changes in illumination angle than smooth surfaces (Cierniewski et al., 2015). Building on these findings, this study investigates whether the same phenomenon systematically manifests in coarser-scale, satellite-derived bare soil reflectance. The observations are compared with a second set of temporally stable, smooth control surfaces, enabling atmospheric effects to be distinguished from surface–light interactions. Compared to soil moisture, the influence of illumination geometry on soil reflectance has received relatively limited attention in the applications that derive soil properties or perform soil monitoring, possibly due to the implicit assumption that Level-2 processing adequately accounts for these effects. However, given the inevitable seasonal variation in solar geometry, this factor represents a potentially important and underexplored source of variability that warrants systematic investigation.

This study aims to:

- quantify the influence of surface soil moisture and illumination geometry on the reflectance of bare-soil surfaces observed by Sentinel-2 and Landsat 8;
- assess the contribution of surface-light interactions on rough bare-soil surfaces

to the observed reflectance variability; and

- investigate the relationship between the effect magnitudes of both drivers and soil texture.

Leveraging a large archive of satellite observations spanning Europe between 2018 and 2024 and integrating complementary datasets, we apply a rigorous statistical framework to isolate and quantify the impact of surface soil moisture and illumination geometry on the observed temporal variability in soil reflectance.

2. Materials

Data used in the analysis combines the temporal variance of multi-spectral satellite observations at LUCAS sampling sites with in situ soil texture information and environmental datasets describing soil moisture, sensor geometry and topology. Together, these datasets enable the investigation of spectral variability across a large number of sites and allow the identification of factors contributing to this variability.

2.1. LUCAS Topsoil Library

The statistical analysis requires a large number of geographically distributed sites with known soil properties. For this purpose, sampling locations of the surveys from the European soil database LUCAS, provided by the European Soil Data Centre, were used (surveys from 2009 up to 2018). Specifically, all 27819 sites specified in the 2018 survey that have soil texture information were selected. The LUCAS sites are distributed across Europe and follow a harmonized sampling pattern. This ensures broad coverage of diverse environmental conditions and soil types.
In addition to the geographic coordinates of the sites, the soil texture (percentages of clay, silt and sand) were incorporated at a later stage of the analysis to interpret the statistical results.

2.2. Remote Sensing Reflectance Data

The main objective of the analysis is to understand the mechanisms that drive the temporal variability of multi-spectral surface reflectance. For this purpose, long-term archives from the Sentinel-2 and Landsat 8 satellite missions were used, which provide consistent multi-spectral observations of the land surface. We focus our analysis on the time between 2018-2024 (7 years) ; the usage of two independent satellite missions reduces mission-specific biases and increases the robustness of the results.

Sentinel-2. Sentinel-2 imagery processed to Level-2A surface reflectance with Sen2Cor was filtered using the Scene Classification Layer (SCL). The filtering steps aim to retain observations where the land surface is clearly visible and not affected by clouds or extreme illumination conditions (we keep vegetation (class 4), bare soils (class 5), or water (class 6)). These classes are retained to avoid prematurely discarding potentially valid bare-soil observations, such as dark or temporarily flooded soils. The final bare-soil selection, including additional filtering to remove pixels affected by residual clouds, haze, and vegetation, is described in Section 3.1. Scenes with a sun zenith angle of more than 70 degrees are ignored, as SentiWiki (2025) discourages from using them for scientific purposes. Scenes with a cloud cover greater than 80% are excluded. In total more than 8 million spectra from 397567 individual Sentinel-2 scenes are part of the statistic. Table 1 lists the spectral bands (all bands resolving at 10 m and 20 m spatial resolution).

Landsat 8. For Landsat 8, surface reflectance with pixels flagged as clear sky (value 21824 or 21888) in the quality (QA) layer were selected. The analysis included the spectral bands as in Table 1 of the Operational Land Imager (OLI). Similar to Sentinel-2, only scenes with less than 80% cloud cover and sun zenith angles below 70 degrees were considered. This includes over 1.7 million individual Landsat spectra from 32386 Landsat 8 scenes. The lower number of Landsat spectra is primarily due to its lower revisit frequency compared with the Sentinel-2 constellation. Scene counts are not directly comparable because Landsat scenes have a larger footprint. At each site, the complete temporal stack of all valid acquisitions, along with metadata, such as acquisition time and sensor geometry, was extracted and stored in NetCDF-4 format to facilitate efficient statistical analysis.

Symbol	Sentinel-2 Band	Landsat 8 Band
ρ_{blue}	B02	B2
ρ_{green}	B03	B3
ρ_{red}	B04	B4
ρ_{re1}	B05	—
ρ_{re2}	B06	—
ρ_{re3}	B07	—
ρ_{nir}	B08	B5
ρ_{nir2}	B8A	—
ρ_{swir1}	B11	B6
ρ_{swir2}	B12	B7

Table 1: Band-symbol mapping for Sentinel-2 MSI and Landsat 8 OLI surface reflectance.

2.3. Surface Moisture

Soil moisture strongly affects the reflectance of bare soils and contributes to the observed temporal variability. In order to estimate the moisture content of the upper layer of the soil, we considered two suitable datasets: 'Copernicus Surface Soil Moisture' and 'ERA5 reanalysis hourly precipitation'.

Copernicus Surface Soil Moisture. The Copernicus Land Monitoring Service Surface Soil Moisture product was used as the primary dataset to quantify soil wetness. The dataset is derived from Sentinel-1 SAR data and covers Europe at a spatial resolution of 1 km. All observations from 2018 to 2024, that coincide with a same-day satellite acquisition (Sentinel-2 or Landsat 8) were included in the analysis (Copernicus Global Land Service, 2018). According to the Land Monitoring Service from Copernicus, it measures "the relative water content of the top few centimeters soil, describing how wet or dry the soil is in its topmost layer, expressed in percent saturation." (Copernicus Land Monitoring Service, 2025). This variable is hereafter denoted as p_{ssm}.

ERA5 hourly precipitation. The ERA5 reanalysis dataset was selected as a secondary data source. Although it does not directly provide soil moisture, it offers hourly precipitation estimates that can be used to quantify antecedent precipitation prior to satellite observations. The dataset has an hourly temporal resolution. ERA5 is produced by the Copernicus Climate Change Service at the European Centre for Medium-Range Weather Forecasts (ECMWF) and the precipitation data for 7 years (2018-2024) was downloaded via the Copernicus Climate Data Store. The data is in mh^{-1} and its spatial resolution is 0.25 degrees (Copernicus Climate Change Service (C3S)). The data was multiplied by a factor of 1000 to obtain a hourly rain in millimeter. A logarithmic transformation was applied to account for its highly skewed distribution to facilitate its use in the linear regression for which it is denoted as p_{era}.

2.4. Auxiliary data

Digital elevation model. Topographic information is needed to compute the sun incidence angle at each LUCAS site. It was derived from the Copernicus Digital Elevation Model (DEM) at 30m resolution. For each study site, the corresponding DEM pixel was identified and its immediate northern, eastern, southern, and western neighbors extracted to characterize the local terrain topology (ESA, 2021).

Location of airport runways. Reflectance measured over paved airport runways was used as a control. Since soil roughness is hypothesized to correlate with sun-angle–induced reflectance variability, runway surfaces provide a useful reference because they are smooth and largely free of shadow-casting objects.
Airport locations were obtained from Natural Earth (2024). Within these airports, runway buffer zones and wide runway intersections were manually identified where the surface extent was sufficient to fully contain a single Landsat 8 or Sentinel-2 pixel without intersecting adjacent land-cover types. This ensures that pixels are spectrally pure. Further, we deliberately avoid touchdown zones where rubber is deposited. In total, 727 locations across 227 airports distributed throughout Europe were selected. In appendix Appendix B the spatial distribution of the control is shown as well as an example of a specific location.

3. Methods

To investigate the variance in time series of Sentinel-2 and Landsat 8 soil surface reflectance, several pre-processing and analysis steps are required. These steps aim to reliably isolate bare soil observations and quantify the environmental and observational factors, that are candidates to contribute to reflectance variability. The methodological workflow consists of the following steps:

- Classification of bare soil pixels in Sentinel-2 and Landsat 8 surface reflectance data (Section 3.1).
- Computation of illumination incidence geometry at each study site (Section 3.2) and extraction of surface soil moisture.
- Estimation of statistical measures that quantify the effect size of different variance components across all study sites (Section 3.3).
- Pooling of local estimates to estimate globally applicable effect magnitudes (random effect meta analysis, Section 3.4)

3.1. Bare soil pixel selection

The selection of bare soil pixels follows the approach proposed by Heiden et al. (2022) and Karlshoefer et al. (2025). The method relies primarily on a spectral index defined as a linear combination of the Normalized Difference Vegetation Index (NDVI, (Urbina-Salazar et al., 2021)) and the Normalized Burn Ratio (NBR, (García and Caselles, 1991)). Due to regional variability in the spectral characteristics of dry vegetation and soil, this spectral index requires region-specific threshold values. To account for this variability, a dynamic threshold map was generated using the HISET algorithm. The algorithm iteratively converges to threshold values maximizing the spectral separation between bare soil surfaces and dry vegetation signals, which represent the two spectrally most similar land surface classes in this context. HISET primarily aggregates pixels within the native Landsat or Sentinel-2 tiling grid. However, if the number of pixels in a given class is insufficient, the aggregation region is expanded by merging adjacent tiles. The resulting threshold values are subsequently smoothed using radial basis function interpolation, with support points located at the centroids of the corresponding grid cells. The final threshold maps for Sentinel-2 and Landsat 8 are provided in the Appendix Appendix A.

If the value of the spectral index falls below the locally derived threshold, the spectra are classified as bare soil without significant influence from dry or green vegetation. The european-wide threshold map for the combined index NDVI+NBR is attached in the appendix Appendix A

. Further refinements were introduced by Karlshoefer et al. (2025), who showed that haze and semi-transparent clouds are not always fully captured by the standard cloud mask and may distort the spectral signature of soil pixels. To mitigate these effects, additional filtering steps were applied. These include the use of an additional spectral index designed to detect haze contamination as well as temporal outlier detection applied along the time series.

The entire processing chain was replicated for Landsat 8 surface reflectance data. This procedure ultimately yielded a seven-year temporal stack of surface reflectance observations, representing bare soil conditions at each LUCAS site, extracted from both the Sentinel-2 and Landsat 8 archives.

3.2. Sun Zenith and Incidence Angle

Variations in solar illumination geometry are a candidate for variability in the surface reflectance spectra. The sun zenith angle (θ_z) is the angle between local zenith at the target and a vector pointing from the target to the sun ; the energy received I per unit area is directly related to its cosine $I = I_0\, cos(\theta_Z)$. Surface orientation $\frac{\partial z}{\partial x}$ and $\frac{\partial z}{\partial y}$ was derived from the DEM using finite differences in the east-west and north-south direction. The surface normal vector $\boldsymbol{n}$ was computed as

$$\boldsymbol{n} = \frac{\left(-\frac{\partial z}{\partial x}, \frac{\partial z}{\partial y}, 1\right)}{\left\| \left(-\frac{\partial z}{\partial x}, \frac{\partial z}{\partial y}, 1\right) \right\|_2}. \tag{1}$$

The solar incidence angle θ_i, representing the angle between the surface normal and the solar beam is the dot product

$$cos(\theta_i) = \boldsymbol{n} \cdot \boldsymbol{s} \tag{2}$$

$\boldsymbol{s}$ being the vector parallel to the sun beam, that is $\boldsymbol{s} = (\sin(\theta_z)\sin(\phi_s), \sin(\theta_z)\cos(\phi_s), \cos(\theta_z))$

3.3. Multivariable Linear Regression

At each site, we applied a multi-variable linear regression model to quantify how the independent variables influence the reflectance of bare soil. The general equation is

$$\boldsymbol{Y} = \beta_0 + \sum_{p=0}^{q} (\beta_p \boldsymbol{X}_p) + \epsilon, \tag{3}$$

where $\boldsymbol{Y}$ is the soil reflectance, $\boldsymbol{X}_p$ the independent variables (e.g. sun incidence angle), β_p their respective coefficients and ϵ the residual error. It is also written $Y \sim X_1 + X_2 + \cdots + X_q$.
Each predictors relative impact is calculated while controlling the other predictors by an analysis of variance (ANOVA). Specifically, the proportion of explained variance caused by any single predictor was quantified by partial eta squared (Cohen, 1973):

$$\eta_P^2 = \frac{\mathrm{SoS_{effect}}}{\mathrm{SoS_{effect}} + \mathrm{SoS_{error}}}. \tag{4}$$

SoS refers to the sum of squares for the effect or its corresponding error term. We chose η_P^2 over alternatives as it is the most commonly used measure of effect size in literature (Richardson, 2011). Conceptually, it is the proportion of total variance of the measured soil reflectance that is uniquely explained by a given independent variable. In addition, we compute the standardized effect size and its standard error (Nieminen, 2022)

$$\beta^* = \frac{\mathrm{std}(\boldsymbol{X})}{\mathrm{std}(\boldsymbol{Y})}\beta \tag{5}$$

$$\mathrm{SE}(\beta^*) = \frac{\mathrm{std}(\boldsymbol{X})}{\mathrm{std}(\boldsymbol{Y})}\mathrm{SE}(\beta) \tag{6}$$

In contrast to the regular regression coefficients, the standardization makes β^* unitless. It explains the impact and direction on the dependent variable when the independent variable is increased by one time its standard deviation.

3.4. Statistics on Multiple Sites

Statistical significance at site. To evaluate the number of sites that exhibit statistical significant correlation, simple aggregation and averaging of site-specific statistics inflate the false positive rate due to multiple hypothesis testing. To reduce the likelihood of rejecting a null hypothesis purely by chance, the Benjamini-Hochberg correction is applied. It controls the false discovery rate by adjusting the thresholds at which a hypothesis tests to be correct or rejected (Benjamini and Hochberg, 2018). This procedure is part of the meta analysis and allows the identification of sites exhibiting statistically robust and consistent effects, that may share a common property and are worth exploring.

Pooled effects. To synthesize global effect estimates across all sites, we employ a meta-analytic framework that explicitly accounts for between-site heterogeneity and statistical power. Individual sampling sites (e.g. LUCAS sites) differ substantially in the number of available satellite observations (e.g. due to different likelihood for clouds at the site) and in the variance of the explanatory variables, resulting in unequal uncertainty of site-level effect estimates. Meta-analysis provides the approach to combine these estimates for each study site by weighting them according to their statistical significance (Borenstein et al., 2009).
The goal is to obtain global estimates of the effect per independent variable, so both η_P^2 and β^* from the previous section are pooled. Note that all sites are included in the pooling procedure, irrespective of individual significance, to avoid selection bias. The values of η_P^2 re converted to signed partial correlations and subsequently Fisher-transformed

$$r_P = \operatorname{sgn}(\beta)\sqrt{\eta_P^2}$$
$$z_i = \frac{1}{2}\ln\left(\frac{1+r_P}{1-r_P}\right)$$

before pooling (Fisher, 1921). The global estimates are obtained using the random effects model of meta-analysis that accounts for intra-site uncertainty and inter-site heterogeneity. As we are expecting significant inter-site heterogeneity due to the vast study area and the multitude of environmental (e.g. meteorological), topological (e.g. soil texture or slope) and possibly even slight systematic difference from the measurements (Borenstein et al., 2009). After pooling, the inverse Fisher-transform projects $\bar{z}$ back to $\bar{\eta}_P^2$.
Furthermore, the heterogeneity across sites is described by the statistic I^2, as proposed by (Higgins and Thompson, 2002). It explains the percentage of variation due

to heterogeneity and not due to random sampling error.

Name	Var	Description	Spatial Resolution
S2 BXX	Y	Sentinel-2 soil reflectance value for any of the bands defined in 2.2	10m or 20m depending on Band
L8 BX	Y	Landsat-8 soil reflectance value for any of the bands defined in 2.2	30m
sia	X_1	Sun Incidence angle at time of acquisition at location of the site 3.2	interpolated from 5km cartesian grid
p_{era5}	X_2	Antecedent total precipitation for 24 hours prior to acquisition 2.3	0.25 deg
p_{ssm}	X_2	Surface soil moisture same-day acquisition 2.3	1km cartesian grid

Table 2: List of dependent and independent variables that are substituted in the linear regression equation for the respective variables.

3.5. The Continental-Scale Analysis

At each site, 32 $((10[\text{S2 Bands}] + 6[\text{L8 bands}]) \times 2[\mathrm{p}_{era5}|\mathrm{p}_{ssm}])$ linear regression models are fitted. Table 2 shows the choices for the dependent variables Y and independent variables X_1 and X_2.
This allows analysis of the effect of changes in soil moisture and illumination geometry per spectral band of the sensors and the effect of soil moisture is studied from 2 different angles.
Since the objective of this study is explanatory inference rather than prediction, models were fitted using the full available dataset at each site. This yields the most precise and reliable site–level effect size estimators: partial eta squared (η_P^2) and the standardized correlation coefficient (β^*). Standard errors (β_{SE}^*) of the standardized coefficients, that are required in the decomposition of variance were computed analytically from the model estimates. Since only sites with at least 30 observations were included, which is sufficient to stabilize within–site sampling variance estimation for the coefficients, bootstrapping was not necessary.
Finally, the large number of study sites enabled a stratified analysis based on the soil texture information provided by the LUCAS dataset, allowing us to investigate whether the effects of the independent variables differ among soil types.

3.6. Interpretation

The contribution of each independent variable to variations in measured soil reflectance is characterized from two perspectives.
First, the pooled standardized correlation coefficient $\bar{\beta}^{*}$, representing effect strength of reflectance to changes in each independent variable. It can also be interpreted as the sensitivity of the reflectance to changes in the predictors. Through normalization the values become unit-less, enabling comparable across predictors within the model.
Second, pooled partial eta squared $\bar{\eta}^2_P$ quantifies the proportion of variance in measured soil reflectance attributable by each predictor (conditional on all other predictors in the model). The distinction between these two is critical because the explanatory power of a variable depends not only on its sensitivity but on its observed variance.
In fact, this variance represented in the data may differ strongly from the variance associated with the underlying physical process, because satellite acquisitions sample non-uniformly in time. For example, sun incidence angle follows a deterministic annual cycle with a well-defined variance. However, non-uniform sampling of soil reflectances driven by cloud cover, weather, or agricultural practices exposing soil only temporarily, results in an uneven representation of this cycle in the observed data.
Consequently, a predictor may exhibit high sensitivity ($\bar{\beta}^{*}$) while its contribution to explained variance $\bar{\eta}^2_P$ is reduced due to range restriction imposed by the data acquisition process.

4. Results

Figure 3 summarizes the pooled proportion of explained variance by each independent variable ($\bar{\eta}^2_P$) and pooled standardized regression coefficients ($\bar{\beta}^{*}$) across the spectral bands of each sensor with prediction intervals derived from the meta analysis. The illumination geometry is described by the sun incidence angle (X_1: sia), whereas the surface soil moisture is estimated by by the Copernicus Surface Soil Moisture product (X_2: p_{ssm}).
Across all bands in both Sentinel-2 and Landsat 8, the sun incidence angle exhibits the strongest effect , with values for $\bar{\eta}^2_P$ between 0.18 and 0.28 and $\bar{\beta}^{*}$ below -0.4. Thus, it explains the larger conditional share of variance in surface reflectance. .
This dominance is consistent throughout the spectrum, although the relative contribution decreases in the SWIR bands (Sentinel-2: B11 and B12 Landsat 8: B7), where soil moisture becomes more influential.
Sensors show broad agreement in the estimated magnitude of the effects. However,

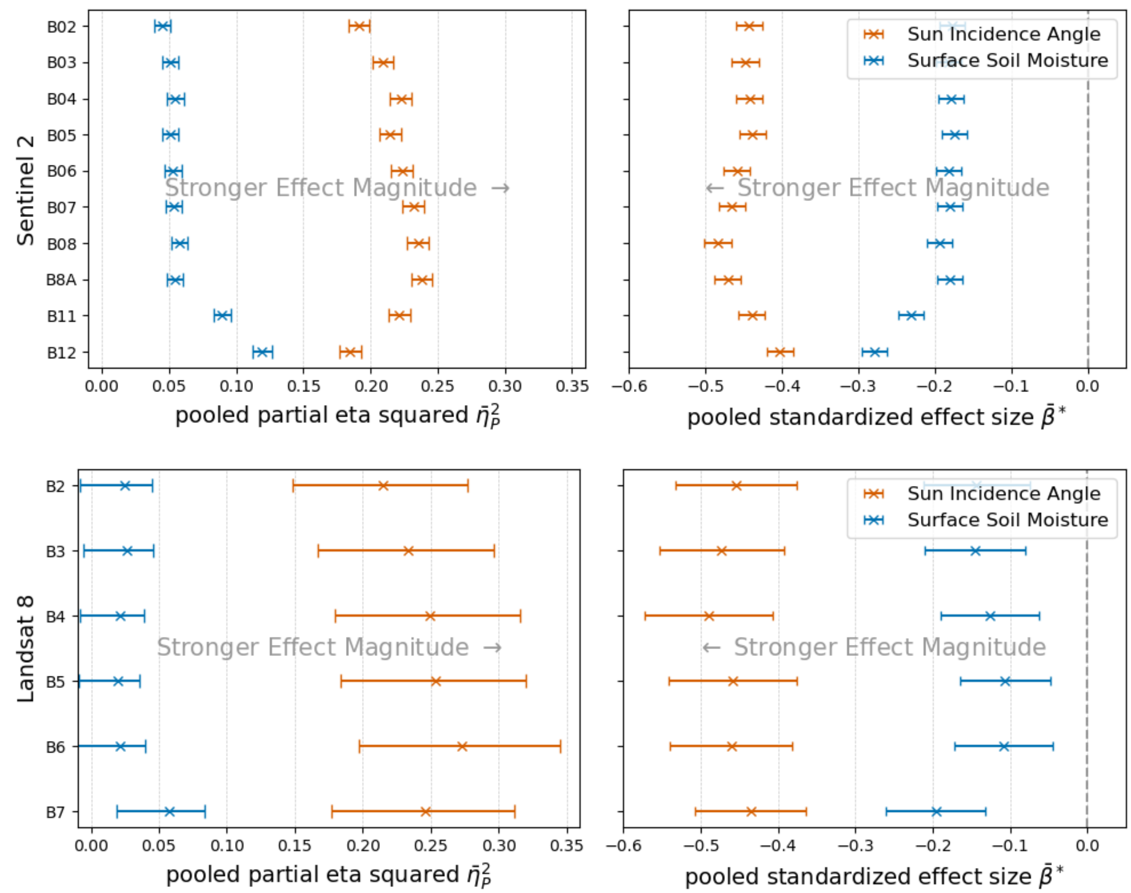

Figure 3: Effect magnitude of predictors p_{ssm} and sia in terms of the proportion of variance attributable to each predictor $\bar{\eta}_P^2$ (left) and the pooled standardized regression coefficient $\bar{\beta}^*$ (right) for Sentinel-2 (top) and Landsat 8 (bottom). Greater magnitudes indicate greater effect size, $\bar{\beta}^*$ also indicates the direction of the effect.

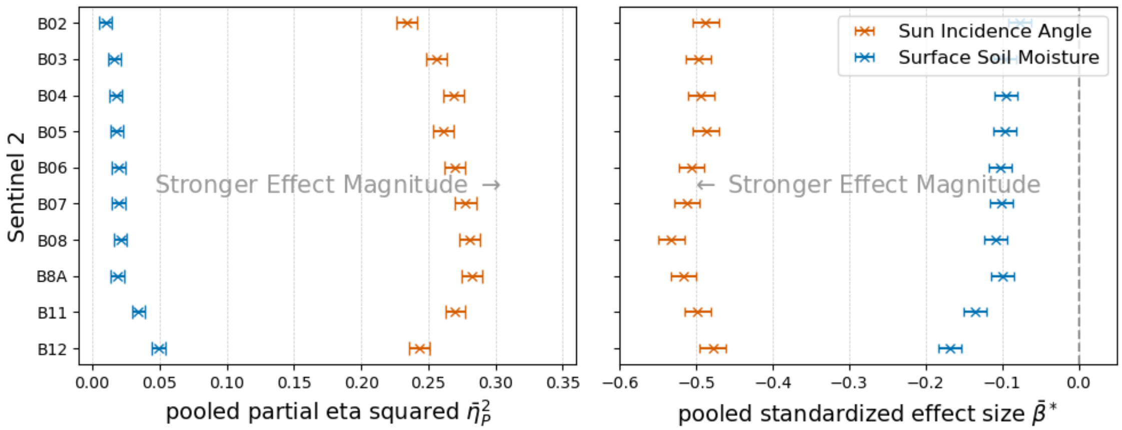

Figure 4: Effect magnitude of predictors p_{era5} and sia in terms of the proportion of variance attributable to each predictor $\bar{\eta}_P^2$ (left) and the pooled standardized regression coefficient $\bar{\beta}^*$ (right) for Sentinel-2. Greater magnitudes indicate greater effect size, $\bar{\beta}^*$ also indicates the direction of the effect.

prediction intervals are generally wider for Landsat 8, indicating greater uncertainty compared to the Sentinel-2 estimates. This difference is primarily attributable to the smaller number of available Landsat 8 observations that coincide with moisture measurements between 2018 and 2024 relative to the Sentinel-2 constellation (see Section 2.2).

The pooled standardized coefficients indicate an increase of one standard deviation in sun incidence angle is associated with a decrease (note the negative sign of $\bar{\beta}^*$) of approximately 0.45 standard deviations in reflectance for both sensors.

Soil moisture also shows a negative relationship with reflectance, though with a smaller effect size than illumination geometry ($\bar{\beta}^*$ between -0.27 and -0.18).

In absolute terms, measured by the unstandardized effect size $\bar{\beta}$, in Band B08, a change of only 1 degree in sun incidence corresponds to an reduction in surface reflectance of $\approx$ 20 Sentinel-2 reflectance units.

A change of 16 degrees in sun incidence angle (that would correspond for sites located at mid-latitudes and in between April 1st and June 1st), corresponds roughly to a change of 1 SD. Then, a reduction of reflectance of up to 0.48 times the standard deviation of the reflectance at the site is likely just caused by the difference in illumination.

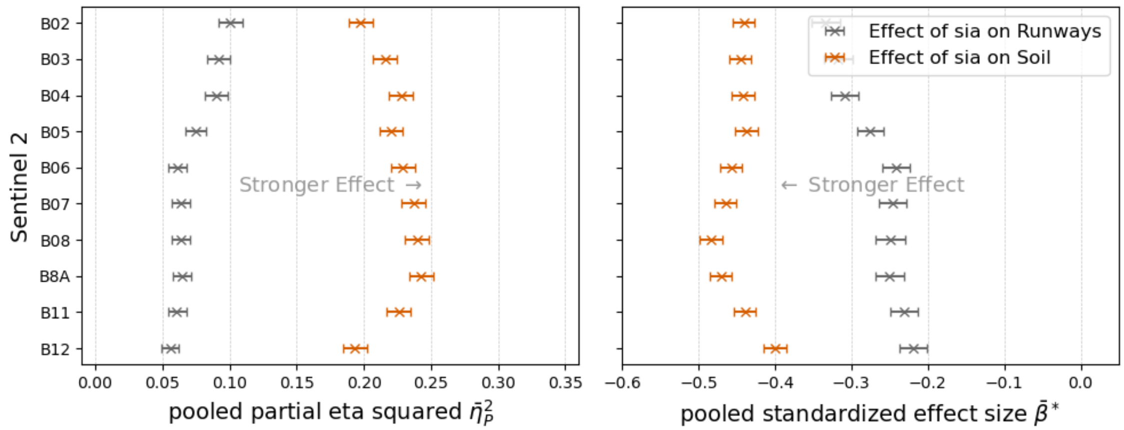

Figure 5: Effect magnitude of the sun incidence angle in terms of partial $\bar{\eta}^2$ (left) and the standardized $\bar{\beta}^*$ (right) with prediction intervals in bare soil and paved surfaces.

4.1. Surface soil moisture estimated by antecedent precipitation

The comparatively weak influence of surface moisture on surface reflectance, relative to illumination geometry as demonstrated in the previous section, is further supported by Figure 4. In this analysis, soil moisture is approximated by antecedent precipitation (p_{era5}) accumulated over the 24 hours preceding satellite acquisition, derived from the ERA5 dataset as described in Section 2.3.
Consistent with previous findings, the moisture proxy explains less variance in reflectance compared to the illumination geometry, while exhibiting a similar overall structure to that shown in Figure 3 (e.g. more influence in the SWIR bands). Note that the prediction intervals are slightly narrower. This originates from the fact that ERA5 data are available for every satellite acquisition, whereas only approximately one third of Sentinel-2 and Landsat 8 observations coincide with same-day Copernicus Surface Soil Moisture measurements, resulting in more data for ERA5 and thus more accurate predictions.

4.2. Shadows in rough Surfaces

As shown in the previous section, the proxy sun incidence angle (sia) exerts the strongest influence on measured soil reflectance throughout the multi-year time series, despite the radiometric corrections applied in the Level-2A surface reflectance products. Therefore, the magnitude of this effect warrants further examination.
Changes in sun incidence angle influence the observed reflectance through two distinct mechanisms. The first mechanism is the *illumination–atmosphere effect*, whereby

increasing sun incidence angles reduce the incoming irradiance per unit area and alter the radiative transfer through the atmosphere (e.g. Rayleigh scattering). These effects are largely accounted for in the Level-2A atmospheric correction (Louis, 2021). The second mechanism is the *surface shadowing effect*. On rough or structured soil surfaces increasing sun incidence angles cause the formation of micro-shadows cast by soil clumps and small-scale surface relief. These shadows reduce the fraction of illuminated surface viewed from nadir as visible to the sensor, thereby lowering the observed reflectance beyond what would be expected from irradiance geometry alone. As micro-shadowing increases, surface scattering deviates progressively from the Lambertian surface assumption underlying the radiometric correction applied in the Level-2A processors.

Analysis using smooth reference surfaces. To separate the two components linked to sun geometry (1. the illumination-atmosphere effect and 2. the surface shadowing effect) we analyzed a dedicated reference dataset from airport runaways described in Section 2.4. The dataset comprises 727 buffer zones at the end of runways and large intersections at 227 major airports across Europe. The sites represent exceptionally stable and homogeneous surfaces that remain unobstructed except for brief periods of aircraft presence, which were removed by using outlier detection. Most importantly, the runway environments are flat and smooth, devoid of nearby objects that could cast shadows or micro-relief.
As shown in Figure 5, both the proportion of explained variance by *sia* ($\bar{\eta}_P^2$) and the standardized regression coefficient ($\bar{\beta}^*$) of the sun incidence angle drop in the control set (here for Sentinel-2 bands). For instance, $\bar{\eta}_P^2$ for B08 is almost 4 times smaller. In all spectral bands, the partial effect of sun incidence angle becomes weaker on smooth, paved surfaces that have similar atmospheric but different surface conditions to bare soil. This confirms that the Sentinel-2 Level-2A illumination correction, done by Sen2Cor compensates mostly for irradiance effects and; therefore by extension, demonstrates, that the strong signal observed over soils in cropland regions cannot be attributed to residual errors in radiometric correction alone.
Instead, the systematic decline in reflectance with increasing sun incidence over rough natural soils must also be linked to the second effect: surface shadowing due to micro-terrain and anisotropic scattering caused by soil roughness.

4.3. Correlation with soil texture

The tendency of soils to form large clumps with more influential shadows depends on the soil texture (e.g. size of particles in the soil that are classified as clay, silt or sand). The large number of sample sites and the presence of soil texture information from the LUCAS survey allowed us to investigate how the standardized effect

sizes vary across percentile stratified subclasses based on the soil texture (as defined in the LUCAS survey (Fernández-Ugalde et al., 2020)). Figure 6 shows the pooled standardized effect sizes $\bar{\beta}^*$ stratified by soil texture. Only a selection of bands from Sentinel-2 ($\rho_{blue}, \rho_{red}, \rho_{nir}, \rho_{swir1}$ and ρ_{swir2}) is shown for clarity; the remaining bands exhibit very similar behavior.
In both sub-figures, the nine steps correspond to deciles between the 5th and 95th percentiles (width indicated by horizontal bars) of the respective texture variable, such that each interval contains a comparable number of sites. Prediction intervals (vertical error bars) are derived from meta-analyses that pool only sites within the corresponding texture interval. The left panel shows the pooled standardized effect sizes of surface reflectance with respect to changes in sun incidence angle as a function of clay content. Larger magnitudes of $\bar{\beta}^*$ indicate a stronger sensitivity of reflectance to changes in sun geometry. Across the spectral domain (five Sentinel-2 bands are shown for clarity), soils with lower clay content exhibit consistently weaker surface shadowing effects. For most bands, the effect magnitude increases with clay content and stabilizes at approximately 30% clay. The right panel shows the pooled standardized effect sizes of surface reflectance with respect to changes in surface soil moisture, stratified by the relative content of sand. Sites with low sand content exhibit substantially stronger moisture effects, whereas increasing sand content is associated with a marked reduction in effect magnitude.
In both plots prediction intervals remain sufficiently narrow across the texture gradient, indicating a robust dependence of the respective effects on soil texture.

5. Discussion

This study examined the relative influence of two drivers of temporal variability in satellite-derived bare-soil reflectance: surface soil moisture and illumination geometry, which governs the interaction of light with the often rough soil surface shaped by land management practices (e.g. tilling, plowing, compaction). Both drivers are well acknowledged in the soil spectroscopy and remote sensing literature (Chabrillat et al., 2019) and have been consistently quantified at continental scale. The analysis was conducted in the context of the applicability and interpretability of soil reflectance composites (e.g. DLR's SoilSuite (Heiden et al., 2024)).

5.1. Impact of soil moisture and soil roughness

Our results place the influence of these drivers into perspective by showing that changes in illumination geometry, and in particular the associated surface shadowing effect, contribute more to temporal soil reflectance variability than changes in surface

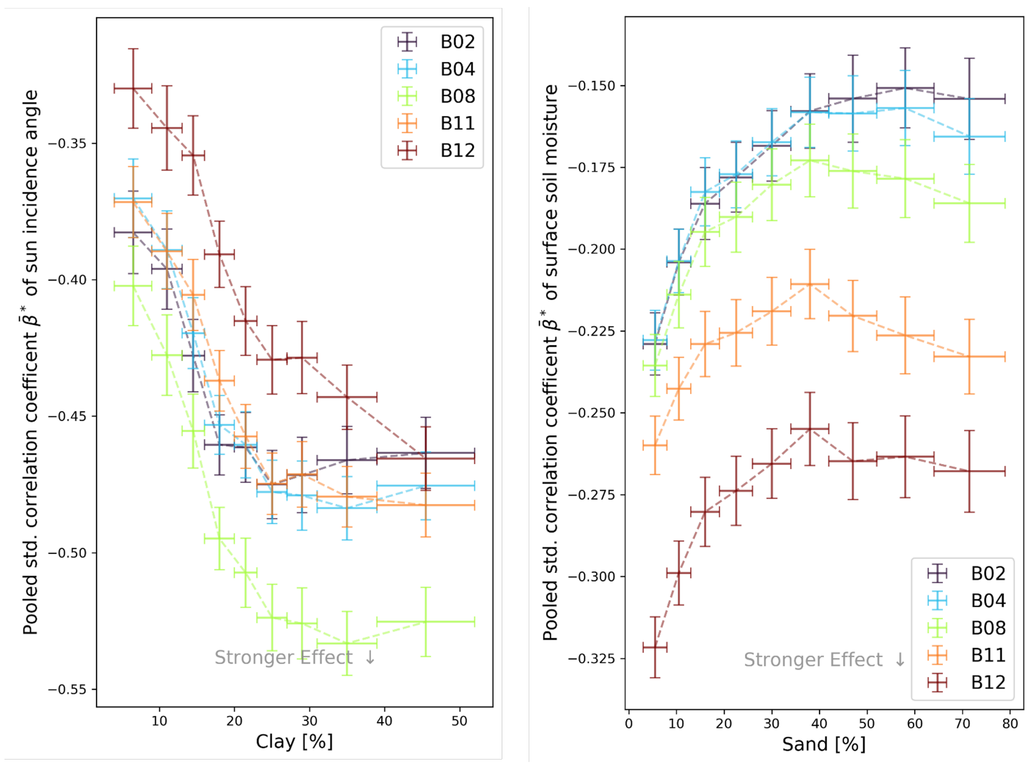

Figure 6: Left: Pooled standardized effect sizes $\bar{\beta}^*$ of surface reflectance of soils with respect to changes in the sun incidence angle (X_1). Percentile-Stratified by the clay content of the soil at the sample site. Right: Similar the effect size $\bar{\beta}^*$ of surface reflectance of soils with respect to changes in surface soil moisture (X_2). Percentile-Stratified by the fraction of sand content at the sites soil. Width of a step represent the interval size of clay / sand content and the error bars are prediction intervals as estimated by the meta analysis that pools only sites with the respective interval.

soil moisture.

One explanation is a sampling bias inherent to optical satellite archives. Moist soil conditions frequently coincide with cloudy or overcast weather, which prevents optical observations. When optical observations are possible they are typically timed before or close to noon (descending node of Sentinel-2 10:30am, of Landsat 8 10:12am (SentiWiki, 2025; NASA, 2026)) and in sunny conditions, the upper soil layer that is sensed by the sensors might dry quickly. As a result, the available satellite archive is biased toward conditions where the upper most surface layer is relatively dry, effectively restricting the observable range of soil moisture variability and limiting the variance that can be attributed to this factor.

This does not contradict compositing approaches that aim to reduce the influence of moist observations (e.g. (Vaudour et al., 2021)), but suggests that this is of secondary importance. The impact of soil wetness on induced variance into the reflectance signal is stronger in the shortwave-infrared (SWIR) region than in the visible or near-infrared ranges. This finding is consistent with radiative transfer models that model the influence of soil moisture content on spectral response and that show that the SWIR range reacts more sensitively to changes in soil moisture contents (Lobell and Asner, 2002) (Bablet et al., 2018).

The strongest effect observed in this study is linked to surface roughness through the surface shadowing effect induced by illumination geometry. This interpretation is supported by the clear separation of the effect magnitudes observed for runways and natural bare-soil surfaces (Figure 5). As shown in Appendix B, the runway sites were selected across Europe to cover the full latitudinal range and the associated seasonal variation in solar elevation.

The magnitude of this effect correlates with soil texture. Clay-rich soils ($> 25\%$ clay), which tend to form larger aggregates or soil clumps (Wagner et al., 2007) and therefore exhibit greater surface micro-relief, show a stronger decline in reflectance with increasing sun incidence angle.

On the other hand, sandy soils, which generally retain less water in the upper soil layer (Mubarak et al., 2009), show weaker responses to changes in the soil moisture. While these relationships appear physically plausible (e.g high water holding capacity of clay-rich soils) and are supported by a large number of observations and study sites, further analyses (e.g., mapping of soil surface roughness in freshly tilled fields with different soil textures) are required to confirm the proposed mechanisms.

Beyond demonstrating that the L2A-corrected soil reflectances of both Sentinel-2 and Landsat 8 remain influenced by illumination geometry, the identified shadowing effect has broader implications: First, understanding the spectral response of soils to changing illumination geometry is directly relevant for improving bidirectional

reflectance distribution function (BRDF) corrections applied to soil surfaces. The results strongly suggest that radiometric corrections based on Lambertian assumptions underestimate these effects. This is consistent with research into the BRDF characteristics of bare soil (Cierniewski and Verbrugghe, 1997) and as noted by Lucht et al. (2000) in this context, "the solar zenith angle dependence of albedo carries information about the surface [...] due to strong shadowing within the pixel".
Therefore, depending on the application, the proposed methodology can be used directly for correction strategies (e.g. parameterized as a function of sun zenith angle and, potentially, soil texture), or, alternatively, it can be used to evaluate different correction strategies that should overall lead to a reduction in the magnitude of the illumination-driven effect.
Second, the strength of the shadowing effect itself may be treated as an informative signal. When Lambertian-based corrections are applied uniformly, the remaining illumination sensitivity in long-term reflectance time series can serve as an indirect indicator of soil surface roughness. While this value is an average over multiple years (here 7 years), it could still provide an insight into soil roughness as a soil property that itself could be linked to soil structure and management practices.
Third, these findings have implications for soil monitoring applications that exploit temporal reflectance observations. Models trained on time series of band-wise reflectance values may misinterpret illumination-induced variability as changes in soil chemistry. In contrast, applications based on spectral shape metrics, such as normalized differences between spectral bands, are expected to be less sensitive because illumination geometry affects all spectral bands.

5.2. Methodological scope and limitations

The analysis combines datasets only when observations were acquired on the same day (e.g., Copernicus SSM and satellite reflectance) to reduce temporal mismatches within the regression. Furthermore, all datasets are retained in their native spatial resolution, avoiding resampling to a common grid. For each study site, the temporal series is always extracted from a series of congruent pixels, such that potential location mismatches between the study site and the corresponding pixels are expected to remain relatively systematic over time rather than varying randomly between acquisitions. Finally, relationships and absolute values are compared only within individual study sites rather across different sites.
Transferring the variance explanation to variance prediction has to be done cautiously. The meta-statistical framework applied in this study is designed to synthesize information across a large number of spatially distributed studies or sites, yielding robust estimates of the average sensitivity of soil reflectance to individual

confounding factors and their typical contributions to spectral variability. However, this approach is not intended to produce a single predictive model that is directly transferable to individual sites. We consistently observed high heterogeneity terms ($I^2 > 50$) across effects indicating substantial between-site variability. As a result, globally pooled effects should not be interpreted as site-specific predictions, but rather as descriptors of dominant processes and their relative importance.

This reasoning is reflected in our choice of statistical framework. Rather than assuming a single common effect across all sites, as in a fixed-effects meta-analysis, we adopt a random-effects approach that allows effect sizes to vary between sites. In this formulation, site-specific effects are treated as realizations from an underlying distribution, thereby explicitly accounting for between-site variability in both baseline reflectance and sensitivity to the considered drivers. Although this approach is mathematically more complex, it is better suited to accommodate the substantial heterogeneity arising from differences in soil properties, climatic conditions, observation geometry, and uneven temporal sampling across sites and seasons.

6. Conclusion

In this study, we demonstrate that variance in time series of Level-2 surface reflectance of bare soil pixels induced by illumination geometry is substantially greater than that associated with soil surface moisture. These findings are statistically robust and exhibit consistent patterns across both Landsat 8 and Sentinel-2 archives. Moreover, the comparatively weak influence of surface moisture was independently corroborated using two external datasets: Copernicus Surface Soil Moisture and ERA5 reanalysis precipitation data. While these relationships are observed across all spectral bands, systematic differences in their magnitude exist. In particular, soil moisture exerts a relatively stronger influence in the shortwave infrared (SWIR) region.

A statistical comparison between bare soil sites and smooth, paved runway sites demonstrates that illumination-driven variance is primarily caused by surface–light interactions, such as shadowing effects on rough soil surfaces and anisotropic scattering behavior. In addition, soil texture modulates the strength of these effects. This relationship may reflect differences in micro-scale surface structure (e.g. aggregation and clumping), although the underlying mechanism was not directly investigated in this study.

The analysis is based on 27,819 sites across Europe over a seven-year period leveraging a substantial portion of the Sentinel-2 and Landsat 8 data archives. Although the findings may not be universally transferable to all regions and soil types, the

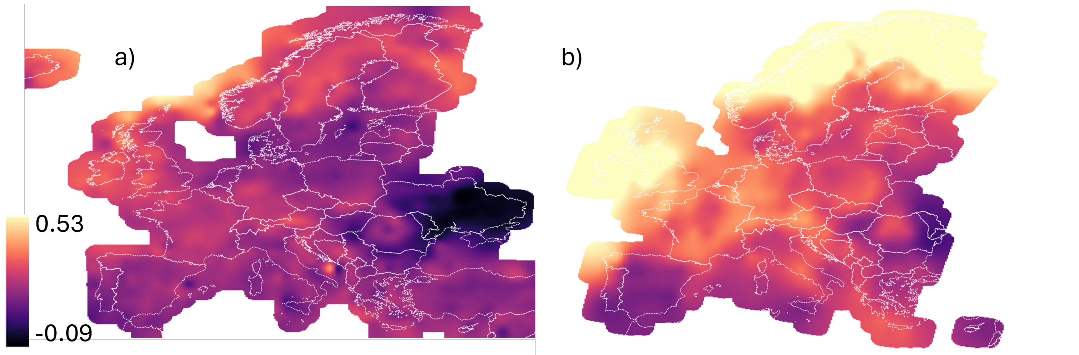

Figure A.7: NDVI+NBR regional threshold maps to select bare soil observations in Sentinel-2 (a) and Landsat 8 (b).

overarching patterns are statistically well supported. These results offer several potential applications: improving BRDF correction approaches for bare soils to reduce illumination-induced variability; exploiting reflectance variability as an informative signal related to soil texture or management practices; and guiding the selection of proxy variables in digital soil mapping.

7. Acknowledgments

This research received funding from the ESA WORLDSOILS project (Contract No. 400131273/20/I-NB) and from the CUP4SOIL project with the action No. 2020-2-14. CUP4SOIL belongs to the FPCUP framework, which is financed by the European Commission, under the FPA no.: 275/G/GRO/COPE/17/10042.

Appendix A. NDVI+NBR Regional Threshold Maps for bare soil selection

Figure A.7 shows the regional threshold maps derived using the HISET algorithm for the combined spectral index NDVI+NBR for Sentinel-2 (left) and Landsat 8 (right). The rasters are publicly available on the Zenodo.

Appendix B. Distribution and Selection of runways

Figure B.8 shows the spatial distribution of the runways. A Geopackage containing all sampled locations is on Zenodo.

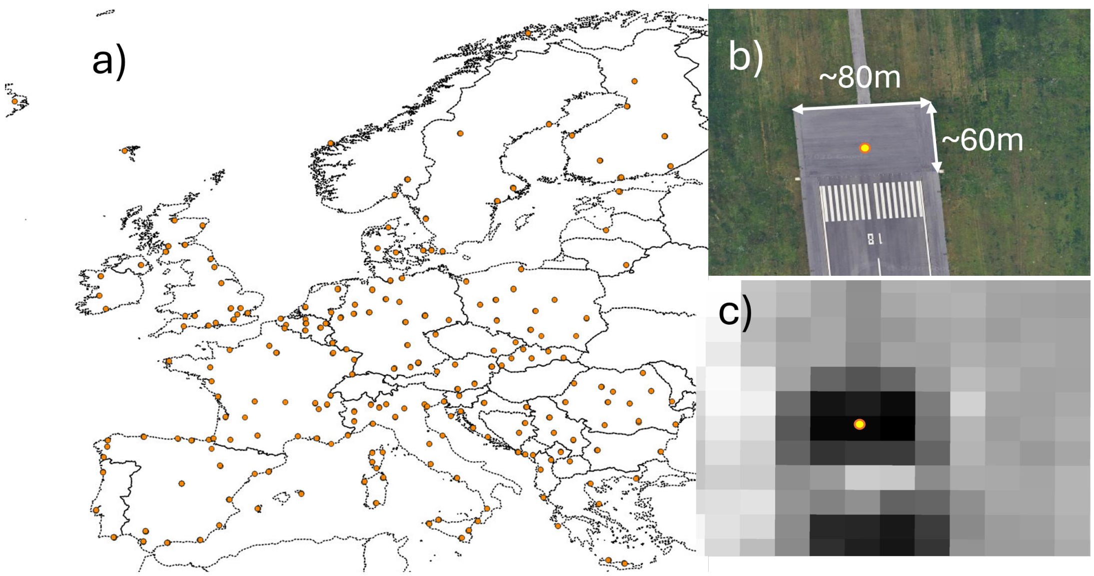

Figure B.8: (a) Spatial distribution of the 227 airports from which 727 locations were manually selected to represent comparatively stable, smooth surfaces compared to bare soil. (b) Example of a frequently selected location: the buffer area preceding the actual runway. (c) Illustration of the spatial relationship between a Sentinel-2 20m resolution and the runway surface, demonstrating that pixels located near the runway center are spectrally pure.

References

Bablet, A., Vu, P., Jacquemoud, S., Viallefont-Robinet, F., Fabre, S., Briottet, X., Sadeghi, M., Whiting, M., Baret, F., Tian, J., 2018. Marmit: A multi-layer radiative transfer model of soil reflectance to estimate surface soil moisture content in the solar domain (400–2500nm). Remote Sensing of Environment 217, 1–17. URL: https://www.sciencedirect.com/science/article/pii/S0034425718303651, doi:https://doi.org/10.1016/j.rse.2018.07.031.

Bachmann, C.M., Philpot, W., Abelev, A., Korwan, D., 2014. Phase angle dependence of sand density observable in hyperspectral reflectance. Remote Sensing of Environment 150, 53–65. URL: https://www.sciencedirect.com/science/article/pii/S0034425714001102, doi:https://doi.org/10.1016/j.rse.2014.03.024.

Badura, G., Bachmann, C.M., 2019. Assessing effects of azimuthally oriented roughness on directional reflectance of sand. IEEE Journal of Selected Topics in Applied Earth Observations and Remote Sensing 12, 1012–1025. doi:10.1109/JSTARS.2019.2896592.

Benjamini, Y., Hochberg, Y., 2018. Controlling the false discovery rate: A practical and powerful approach to multiple testing. Journal of the Royal Statistical Society: Series B (Methodological) 57, 289–300. URL: https://doi.org/10.1111/j.2517-6161.1995.tb02031.x, doi:10.1111/j.2517-6161.1995.tb02031.x.

Borenstein, M., Hedges, L.V., Higgins, J.P., Rothstein, H.R., 2009. Introduction to Meta-Analysis. John Wiley & Sons, West Sussex.

Box, G.E.P., Jenkins, G.M., Reinsel, G.C., Ljung, G.M., 2015. Time Series Analysis: Forecasting and Control. 5th ed., Wiley.

Broeg, T., Don, A., Scholten, T., Erasmi, S., 2025. Bare soil composite for germany (10 m) based on sentinel-2 data from 2015 to 2024. URL: https://doi.org/10.5281/zenodo.15402687, doi:10.5281/zenodo.15402687.

Castaldi, F., Chabrillat, S., Don, A., van Wesemael, B., 2019. Soil organic carbon mapping using lucas topsoil database and sentinel-2 data: An approach to reduce soil moisture and crop residue effects. Remote Sensing 11. URL: https://www.mdpi.com/2072-4292/11/18/2121, doi:10.3390/rs11182121.

Chabrillat, S., Ben-Dor, E., Cierniewski, J., Gomez, C., Schmid, T., van Wesemael, B., 2019. Imaging spectroscopy for soil mapping and monitoring. Surveys in Geophysics 40, 361–399. URL: https://doi.org/10.1007/s10712-019-09524-0, doi:10.1007/s10712-019-09524-0.

Cierniewski, J., Kaźmierowski, C., Królewicz, S., 2015. Evaluation of the effects of surface roughness on the relationship between soil brf data and broadband albedo. IEEE Journal of Selected Topics in Applied Earth Observations and Remote Sensing 8, 1528–1533. doi:10.1109/JSTARS.2014.2361924.

Cierniewski, J., Verbrugghe, M., 1997. Influence of soil surface roughness on soil bidirectional reflectance. International Journal of Remote Sensing 18, 1277–1288. URL: https://doi.org/10.1080/014311697218412, doi:10.1080/014311697218412, arXiv:https://doi.org/10.1080/014311697218412.

Cohen, J., 1973. Eta-squared and partial eta-squared in fixed factor anova designs. Educational and Psychological Measurement 33, 107–112. URL: https://doi.org/10.1177/001316447303300111, doi:10.1177/001316447303300111, arXiv:https://doi.org/10.1177/001316447303300111.

Copernicus Climate Change Service (C3S), . Era5 hourly data on single levels from 1940 to present. doi:https://doi.org/10.24381/cds.adbb2d47. accessed: 2025-10-10".

Copernicus Global Land Service, 2018. Surface soil moisture (ssm) 1 km daily global, version 1.0. URL: https://doi.org/10.2909/e934b15f-7d48-4c6d-a9c6-6484488aa58f, doi:10.2909/e934b15f-7d48-4c6d-a9c6-6484488aa58f. edition 1.0, created and published 2018-12-18, citation identifier: clms_r_4326_1_km_ssm-daily-global_p_2014-now_v1_r00.

Copernicus Land Monitoring Service, 2025. Surface soil moisture. URL: https://land.copernicus.eu/en/products/soil-moisture/daily-surface-soil-moisture-v1.0. accessed: 31 October 2025.

Demattê, J.A., Rizzo, R., Rosin, N.A., Poppiel, R.R., Novais, J.J.M., Amorim, M.T.A., Rodriguez-Albarracín, H.S., Rosas, J.T.F., dos Anjos Bartsch, B., Vogel, L.G., Minasny, B., Grunwald, S., Ge, Y., Ben-Dor, E., Gholizadeh, A., Gomez, C., Chabrillat, S., Francos, N., Fiantis, D., Belal, A., Tsakiridis, N., Kalopesa, E., Naimi, S., Ayoubi, S., Tziolas, N., Das, B.S., Zalidis, G., Francelino, M.R., de Mello, D.C., Hafshejani, N.A., Peng, Y., Ma, Y., Coblinski, J.A., Wadoux, A.M.C., Savin, I., Malone, B.P., Karyotis, K., Milewski, R., Vaudour, E., Wang, C., Salama, E.S.M., Shepherd, K.D., 2025. A global soil spectral grid based on space sensing. Science of The Total Environment 968, 178791. URL: https://www.sciencedirect.com/science/article/pii/S0048969725004267, doi:https://doi.org/10.1016/j.scitotenv.2025.178791.

ESA, 2015. Sentinel-2 user handbook. None .

ESA, 2021. Copernicus dem – global and european digital elevation model (glo-30). URL: https://doi.org/10.5270/ESA-c5d3d65, doi:10.5270/ESA-c5d3d65.

Fernández-Ugalde, O., Ballabio, C., Lugato, E., Scarpa, S., Jones, A., 2020. Assessment of changes in topsoil properties in lucas samples between 2009/2012 and 2015 surveys. Publications Office of the European Union doi:10.2760/5503.

Fisher, R.A., 1921. On the “probable error” of a coefficient of correlation deduced from a small sample. Metron 1, 210. See equation (V) on p. 210 for the relationship between r and z.

García, M.L., Caselles, V., 1991. Mapping burns and natural reforestation using thematic mapper data. Geocarto International 6, 31–37. doi:10.1080/10106049109354290.

Heiden, U., D’Angelo, P., Karlshoefer, P., 2024. Soilsuite europe. URL: https://geoservice.dlr.de/web/datasets/soilsuite_eur_5y, doi:"10.15489/qkud8cudg596".

Heiden, U., d’Angelo, P., Schwind, P., Karlshöfer, P., Müller, R., Zepp, S., Wiesmeier, M., Reinartz, P., 2022. Soil reflectance composites—improved thresholding and performance evaluation. Remote Sensing 14. doi:10.3390/rs14184526.

Higgins, J., Thompson, S., 2002. Quantifying heterogeneity in a meta-analysis. Statistics in Medicine .

Karlshoefer, P., d’Angelo, P., Eberle, J., Heiden, U., 2025. Evaluation framework for the generation of continental bare surface reflectance composites. Geoderma 459, 117340. URL: https://www.sciencedirect.com/science/article/pii/S0016706125001788, doi:https://doi.org/10.1016/j.geoderma.2025.117340.

Lesaignoux, A., Fabre, S., Briottet, X., 2013. Influence of soil moisture content on spectral reflectance of bare soils in the 0.4-14 ym domain. International Journal of Remote Sensing 34, 2268–2285. doi:10.1080/01431161.2012.743693.

Lobell, D., Asner, G., 2002. Moisture effects on soil reflectance. Soil Science Society of America Journal 66, 722–727. doi:10.2136/sssaj2002.7220.

Louis, J., 2021. Sentinel-2 Level-2A Algorithm Theoretical Basis Document (ATBD). Technical Report S2-PDGS-MPC-ATBD-L2A. European Space Agency (ESA). URL: https://step.esa.int/thirdparties/sen2cor/. sen2Cor Level-2A Processor.

Lucht, W., Roujean, J.L., Schmugge, T., 2000. An algorithm for the retrieval of albedo from space using semiempirical brdf models. Remote Sensing of Environment 72, 339–354. doi:10.1016/S0034-4257(00)00047-2.

McGuirk, S.L., Cairns, I.H., 2024. Relationships between soil moisture and visible–nir soil reflectance: A review presenting new analyses and data to fill the gaps. Geotechnics 4, 78–108. URL: https://www.mdpi.com/2673-7094/4/1/5, doi:10.3390/geotechnics4010005.

Mu, T., Liu, G., Yang, X., Yu, Y., 2023. Soil-moisture estimation based on multiple-source remote-sensing images. Remote Sensing 15. URL: https://www.mdpi.com/2072-4292/15/1/139, doi:10.3390/rs15010139.

Mubarak, A., Ragab, O.E., Ali, A.A., Hamed, N.E., 2009. Short-term studies on use of organic amendments for amelioration of a sandy soil. African Journal of Agricultural Research 4, 621–627.

Mulder, V., de Bruin, S., Schaepman, M., Mayr, T., 2011. The use of remote sensing in soil and terrain mapping — a review. Geoderma 162, 1–19. URL: https://www.sciencedirect.com/science/article/pii/S0016706110003976, doi:https://doi.org/10.1016/j.geoderma.2010.12.018.

NASA, 2026. Landsat 8. https://science.nasa.gov/mission/landsat-8/. URL: https://science.nasa.gov/mission/landsat-8/. accessed: 2026-03-31.

Natural Earth, 2024. Airports — 1:10m cultural vectors. https://www.naturalearthdata.com/downloads/10m-cultural-vectors/airports/. Accessed: 2025-10-22.

Nieminen, P., 2022. Application of standardized regression coefficient in meta-analysis. BioMedInformatics 2, 434–458. URL: https://www.mdpi.com/2673-7426/2/3/28, doi:10.3390/biomedinformatics2030028.

Richardson, J.T., 2011. Eta squared and partial eta squared as measures of effect size in educational research. Educational Research Review 6, 135–147. URL: https://www.sciencedirect.com/science/article/pii/S1747938X11000029, doi:https://doi.org/10.1016/j.edurev.2010.12.001.

Rogge, D., Bauer, A., Zeidler, J., Mueller, A., Esch, T., Heiden, U., 2018. Building an exposed soil composite processor (scmap) for mapping spatial and temporal characteristics of soils with landsat imagery (1984–2014). Remote Sensing of Environment 205, 1–17. URL: https://www.sciencedirect.com/science/article/pii/S003442571730514X, doi:https://doi.org/10.1016/j.rse.2017.11.004.

Sadeghi, M., Babaeian, E., Tuller, M., Jones, S.B., 2017. The optical trapezoid model: A novel approach to remote sensing of soil moisture applied to sentinel-2 and landsat-8 observations. Remote Sensing of Environment 198, 52–68. URL: https://www.sciencedirect.com/science/article/pii/S0034425717302493, doi:https://doi.org/10.1016/j.rse.2017.05.041.

SentiWiki, E.S.A.E.., 2025. S2 products – maximal sun-zenith angle. Web page. URL: https://sentiwiki.copernicus.eu/web/s2-products#S2Products-MaximalSun-ZenithAngle. accessed:2025-10-23.

UN, F., 2024. Soils, where food begins. https://www.fao.org/newsroom/detail/soils-where-food-begins/en. Accessed: 2025-01-21. Soils are the foundation of agri-food systems and about 95% of global food is produced on soils.

Urbina-Salazar, D., Vaudour, E., Baghdadi, N., Ceschia, E., Richer-de Forges, A.C., Lehmann, S., Arrouays, D., 2021. Using sentinel-2 images for soil organic carbon content mapping in croplands of southwestern france. the usefulness of sentinel-1/2 derived moisture maps and mismatches between sentinel images and sampling dates. Remote Sensing 13. URL: https://www.mdpi.com/2072-4292/13/24/5115, doi:10.3390/rs13245115.

U.S. Geological Survey, 2025. Landsat 8–9 Calibration and Validation (Cal/Val) Algorithm Description Document (ADD). Technical Report. U.S. Department of the Interior, U.S. Geological Survey. Landsat 8–9 Calibration and Validation (Cal/Val) Algorithm Description Document.

USGS, 2019. Landsat 8 data users handbook. None .

Vaudour, E., Gomez, C., Lagacherie, P., Loiseau, T., Baghdadi, N., Urbina-Salazar, D., Loubet, B., Arrouays, D., 2021. Temporal mosaicking approaches of sentinel-2 images for extending topsoil organic carbon content mapping in croplands. International Journal of Applied Earth Observation and Geoinformation 96, 102277. URL: https://www.sciencedirect.com/science/article/pii/S030324342030920X, doi:https://doi.org/10.1016/j.jag.2020.102277.

Wagner, S., Cattle, S., Scholten, T., 2007. Soil-aggregate formation as influenced by clay content and organic-matter amendment. Journal of Plant Nutrition and Soil Science 170, 173 – 180. doi:10.1002/jpln.200521732.